# Oxide Defect Engineering Enables to Couple Solar Energy into Oxygen Activation

Ning Zhang,[†] Xiyu Li,[†] Huacheng Ye, Shuangming Chen, Huanxin Ju, Daobin Liu, Yue Lin, Wei Ye, Chengming Wang, Qian Xu, Junfa Zhu, Li Song, Jun Jiang,* and Yujie Xiong*

Hefei National Laboratory for Physical Sciences at the Microscale, iChEM (Collaborative Innovation Center of Chemistry for Energy Materials), School of Chemistry and Materials Science, Hefei Science Center (CAS), and National Synchrotron Radiation Laboratory, University of Science and Technology of China, Hefei, Anhui 230026, P. R. China

S Supporting Information

ABSTRACT: Modern development of chemical manufacturing requires a substantial reduction in energy consumption and catalyst cost. Sunlight-driven chemical transformation by metal oxides holds great promise for this goal; however, it remains a grand challenge to efficiently couple solar energy into many catalytic reactions. Here we report that defect engineering on oxide catalyst can serve as a versatile approach to bridge light harvesting with surface reactions by ensuring species chemisorption. The chemisorption not only spatially enables the transfer of photoexcited electrons to reaction species, but also alters the form of active species to lower the photon energy requirement for reactions. In a proof of concept, oxygen molecules are activated into superoxide radicals on defect-rich tungsten oxide through visible-near-infrared illumination to trigger organic aerobic couplings of amines to corresponding imines. The excellent efficiency and durability for such a highly important process in chemical transformation can otherwise be virtually impossible to attain by counterpart materials.
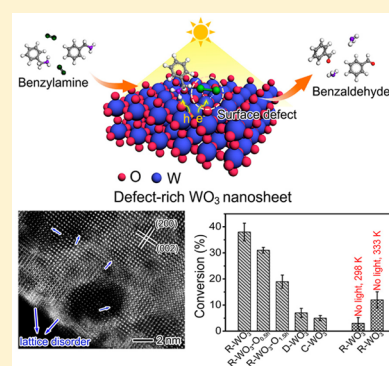
INTRODUCTION

The global energy and resource crisis calls for the development of chemical manufacturing toward minimal energy consumption and catalyst cost. Sunlight-driven reactions, which may replace the conventional thermal-based chemical process, hold great promise to substantially reduce the energy consumption in modern chemical industry.[1−4] In principle, sunlight can be harvested by semiconductor materials or plasmonic noble metal nanocrystals, which creates excitons or hot carriers to turn on chemical reactions on the catalyst surface.[5−7] Among the light-harvesting materials, oxide semiconductor represents a promising candidate for reducing catalyst cost. Unfortunately, despite their widespread application in photocatalytic water splitting,[8] oxide materials have not played a versatile role in the development of light-driven organic synthesis. A variety of classic organic reactions, including but not limited to epoxidation, hydrocarbon oxidation, alcohol oxidation, and aerobic coupling, generally involve the activation of molecular oxygen which typically takes place through the catalysis by noble metals or with thermal energy.[9−11]

To enable light-driven oxygen activation, the solar-to-chemical energy conversion process on oxide catalysts, whose efficiency relies on the energy coupling between photons, excitons and dioxygen species,[12,13] should be certainly better harnessed. During the stepwise process, the solar harvesting responsible for photon-exciton energy conversion can be readily optimized by engineering band structures, such as creation of defect states[14−16] and formation of heterojunctions.[17] Rather, the challenge to energy coupling lies mainly in

the step of energy transfer from excitons to dioxygen species. Specifically the limitation for this key step originates from two bottlenecks. First, molecular oxygen interacts with coordinatively saturated oxide surface mainly through physical adsorption, so as to spatially defer the electron transfer from oxide to oxygen species. Second, most oxide semiconductors that can harvest the majority of solar light, visible and near-infrared (NIR) photons, possess relatively low conduction band edge, so the photoexcited electrons are often incapable of producing highly active oxygen species.

Herein, we demonstrate that defect engineering for tungsten oxide (WO_3), which ensures the chemisorption of molecular oxygen to WO_3 surface, can overcome the above bottlenecks. The chemisorption spatially builds up a channel for the delivery of photoexcited electrons to dioxygen species (O_2), as well as forms superoxide radicals in a chemisorbed state (O_2^{*-}) upon receiving the electrons. With identical oxidative capability to free superoxide radicals ($O_2^{\bullet-}$), the O_2^{*-} radicals can efficiently react with the hole-charged substrate molecules located at the neighbor sites. As such, this pathway no longer requires photon energy to meet the thermodynamic requirement for free O_2/$O_2^{\bullet-}$ pair, and achieves to utilize the solar energy in visible-NIR region toward O_2 activation, which can otherwise be virtually impossible to attain by counterpart materials. Profiting from the chemisorption and activation of molecular oxygen on surface defects, the defect-rich WO_3 can serve as an efficient
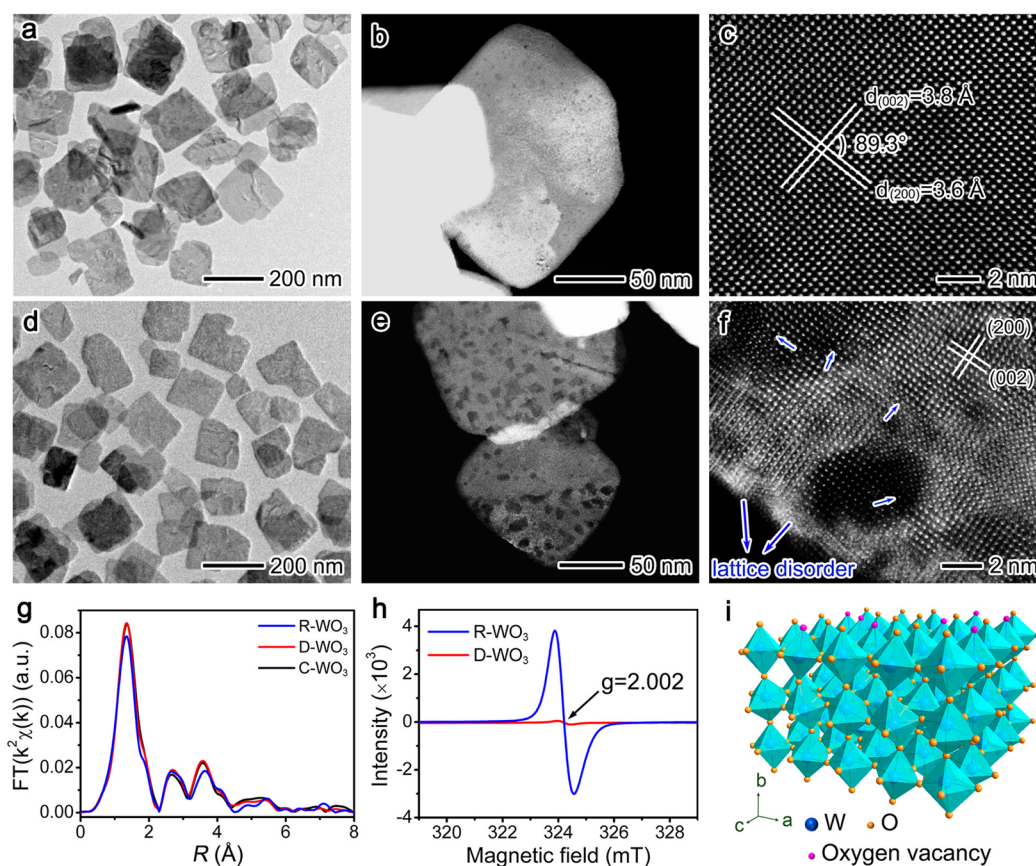
Figure 1. Structure characterization for the defect-controlled WO_3 samples. (a) TEM, (b) STEM, and (c) atomic-resolution HAADF-STEM images of defect-deficient WO_3 (D-WO_3) nanosheets. (d) TEM, (e) STEM, and (f) atomic-resolution HAADF-STEM images of defect-rich WO_3 (R-WO_3) nanosheets. The lattice disorder induced by defects is marked by blue arrows. (g) Fourier-transform W L_3-edge EXAFS spectra of the samples in reference to commercial WO_3. (h) Room-temperature ESR spectra. (i) Schematic illustrating the locations of oxygen vacancies in WO_3 lattice.

photocatalyst for aerobic couplings of primary amines to corresponding imines at room temperature. Moreover, disruptively to the common sense, the defect-rich oxides exhibit long-term durability in the O_2 activation and well maintain the photocatalytic activity during the aerobic couplings.

■ EXPERIMENTAL SECTION

Synthesis of Defect-Controlled WO_3 Nanosheets. Defect-controlled WO_3 nanosheets were synthesized by a two-step process. Briefly, defective $WO_3 \cdot H_2O$ nanosheets were first prepared as a precursor through a mild hydrothermal method. Details are described in the Supporting Information. Then the defect-rich WO_3 (R-WO_3) nanosheets were synthesized by calcining the $WO_3 \cdot H_2O$ powder at 673 K with a heating rate of 2 K·min^{-1} in N_2 atmosphere for 2 h. After cooled to room temperature, the obtained dark-blue powder was collected for further use and characterization. The defect-deficient WO_3 (D-WO_3) nanosheets were formed by following the same calcination method except for the use of air atmosphere, which yielded light-green powder. To control the concentrations of oxygen vacancies, the R-WO_3 sample was recalcined at 623 K in the air for 0.5 or 1.5 h to partially oxidize the defects. The samples were named R-WO_3−$O_{0.5h}$ and R-WO_3−$O_{1.5h}$, respectively.

Synchrotron-Radiation Characterization. Synchrotron radiation photoemission spectroscopy (SRPES) and X-ray photoelectron spectroscopy (XPS) experiments were performed at the Catalysis and Surface Science Endstation in National Synchrotron Radiation Laboratory (NSRL), Hefei. The valence-band spectra were measured using synchrotron-radiation light as the excitation source with photon energy of 40.00 eV and referenced to the Fermi level ($E_F = 0$)

determined from Au. A sample bias of −10 V was applied in order to observe the secondary electron cutoff. The work function (Φ) was determined by the difference between the photon energy and the width of whole valence-band spectra. XPS spectra were collected using monochromatic Al $K\alpha$ X-ray as the excitation source. W L_3-edge extended X-ray absorption fine structure (EXAFS) spectroscopy measurements were performed at the beamline BL14W1 of Shanghai Synchrotron Radiation Facility (SSRF). The electron beam energy of the storage ring was 3.5 GeV with a maximum stored current of 300 mA. O K-edge near-edge X-ray absorption fine structure (NEXAFS) spectroscopy measurements were performed at the soft X-ray beamline 4B7B in Beijing Synchrotron Radiation Facility (BSRF). The electron beam energy of the storage ring was 2.2 GeV with a maximum stored current of 250 mA. The O K-edge spectra were collected in the total electron yield (TEY) mode.

Detection of Superoxide Radical Anion ($O_2^{\bullet-}$). $O_2^{\bullet-}$ was captured using 5, 5-dimethyl-1-pyrroline N-oxide (DMPO). In typical measurements, 5 mg of sample was dispersed in 2.5 mL of methanol which had been bubbled with oxygen for 30 min, and was vigorously shaken for 10 s followed by the addition of 30 μL DMPO methanol solution (0.2 M). The mixture was irradiated using a 300 W Xe lamp for 30 s, and then was analyzed by ESR.

Catalytic Measurements for Aerobic Couplings of Amines. The light-driven catalytic reactions were carried out in acetonitrile (CH_3CN) solution in O_2 atmosphere (1 atm) at room temperature. Typically, 0.1 mmol of substrate and 20 mg of catalyst were dispersed in 4 mL of CH_3CN in a quartz tube, which was then saturated with pure O_2 and sealed with a glass stopper. The suspension was vigorous stirred, and irradiated by a 300 W Xe lamp (Solaredge 700, China) with a 400 nm long-wave-pass cutoff filter (i.e., $\lambda > 400$ nm) and a homemade thermostatic control device at 298 K. The power density

was measured to be 100 mW·cm^{-2}. The 700 nm-cutoff experiments were performed under the same condition by switching the filters. After the irradiation, WO$_3$ catalyst was removed by filtration, and the resultant solution was analyzed by gas chromatography–mass spectrometry (GC-MS, 7890A and 5975C, Agilent) using benzotrifluoride as the internal standard. The thermally driven reactions were performed at certain temperatures by excluding the environmental light with aluminum foil.

First-Principles Simulations. Spin-polarized density functional theory (DFT) simulations were performed with the Vienna ab initio simulation (VASP) package. Perdew–Burke–Ernzerhof (PBE) exchange-correlation functional within a generalized gradient approximation (GGA) and the projector augmented-wave (PAW) potential were employed, and densities of states (DOS) were computed with HSE06 functional. The monoclinic structure of WO$_3$ with 8 W and 24 O atoms in a primary unit cell was built for lattice simulation. The calculated lattice parameters are $a = 7.49$, $b = 7.66$, $c = 7.84$ (Å), and $\beta = 90.3°$. Mono-oxygen defect was modeled by removing one oxygen atom from a unit cell. There are two types of W−O bonds in the lattice, and geometry optimization confirms our experimental finding that the removal of oxygen from the longer W−O−W chain is the most thermodynamically favorable. A system of 2 × 2 slab with four layers was employed to model the WO$_3$ (010) surface, with oxygen atom terminated. Three top layers were relaxed from the bulk positions during the geometry optimizing. The periodic boundary condition was set with a 18 Å vacuum region above surface. Charge distributions were analyzed with the Bader's model. The differential charge density were plotted with the isosurface value of 0.001 e/Å^3, while that for electronic wave function population is 0.007 e/Å^3.

■ RESULTS AND DISCUSSION

Oxygen vacancies originating from defect engineering on oxide surface can provide coordinatively unsaturated (CUS) sites for molecular adsorption, as commonly recognized in thermal-based catalysis.[18] In our proof-of-concept demonstration, we employed WO$_3$ nanosheets as a model material to carry out the defect engineering. The two-dimensional model supplies abundant CUS sites for surface reactions, as well as offers high precision for spectroscopic characterizations by reducing the signals from bulk. The WO$_3$ nanosheets were synthesized by calcining the defective WO$_3$·H$_2$O precursor. The WO$_3$·H$_2$O precursor exhibits a sheet-like morphology and contains numerous defects (Figure S1). Figure 1a−c shows the structure of the sample obtained through a calcination on the WO$_3$·H$_2$O precursor in the air, characterized by transmission electron microscopy (TEM) and aberration-corrected high-angle annular dark-field scanning transmission electron microscopy (HAADF-STEM). The WO$_3$ nanostructures well inherit the sheet-like morphology from their WO$_3$·H$_2$O precursor (Figure 1a and b). As presented in atomic-resolution HAADF-STEM image (Figure 1c), the nanosheet shows continuous and ordered lattice fringes with the lattice spacings of 3.8 and 3.6 Å and the crystal plane angle of 89.3°, which correspond to the (002) and (200) planes, respectively, according to the lattice parameters of monoclinic tungsten oxide (JCPDS No. 83-0951). On account of the sheetlike morphology, it can be deduced that the WO$_3$ nanosheets are mostly enclosed by (010) faces. During the calcination, the oxygen in the air filled into the defects so as to minimize the concentration of oxygen vacancies. As a result, the defect-deficient WO$_3$ nanostructures (namely, D-WO$_3$) exhibit a relatively flat and smooth surface. Moreover, the ordered lattice and smooth surface were still well maintained even at the edge of the sample (Figure S2), further demonstrating the deficiency of defects. By altering the calcination atmosphere to nitrogen, due to the absence of oxygen, the defects in the precursor were largely remained to

produce defect-rich WO$_3$ nanostructures (namely, R-WO$_3$). As revealed by the images (Figure 1d and e), the R-WO$_3$ sample contains numerous small pits. The creation of pits on surface dramatically boosts surface area (Figure S3 and Table S1), which would offer more CUS sites for catalytic reactions. Concomitant with the pits, slight lattice disorder and dislocation have been locally observed in the nanosheets (Figures 1f and S2), highlighting the existence of numerous defects. Despite their varied defects, both samples similarly possess a monoclinic WO$_3$ phase (JCPDS No. 83-0951, Figure S4) and inherit a sheetlike morphology from their precursor (Figure S5).

To directly resolve oxygen vacancies, we employed a set of advanced spectroscopic techniques to characterize the defect-controlled nanosheets, using the commercial WO$_3$ with rare defects (namely, C-WO$_3$, Figure S6) as a reference. Synchrotron radiation-based X-ray absorption fine structure (XAFS) spectroscopy is a powerful element-specific tool to examine local structure. Figure 1g shows the W L$_3$-edge extended XAFS (EXAFS) spectra acquired through a Fourier-transform from the raw data in Figure S7. Apparently R-WO$_3$ displays the shifted peaks with lower intensities compared with C-WO$_3$ and D-WO$_3$, indicating their different local atomic arrangements. To look into bonding situation, we extracted W−O bond lengths and W coordination numbers from EXAFS curve fitting (Table 1). In the monoclinic WO$_3$ lattice, distorted

Table 1. Fitting Results of W L$_3$-Edge EXAFS Data^a

sample	W−O bond	R (Å)	N	σ^2 (10^{-3} Å^2)	ΔE_0 (eV)
R-WO$_3$	W−O$_1$	1.75	4.0	4.6	1.4
	W−O$_2$	2.12	1.4	6.0	12.8
D-WO$_3$	W−O$_1$	1.75	4.2	4.5	2.5
	W−O$_2$	2.11	1.8	5.7	10.9
C-WO$_3$	W−O$_1$	1.75	4.0	4.2	2.3
	W−O$_2$	2.12	2.0	5.1	10.3

^{a}The lengths of W−O bonds and coordination numbers of W atoms were extracted from EXAFS curve-fitting for R-WO$_3$, D-WO$_3$, and C-WO$_3$. R, the length of W−O bonds; N, the coordination number of W atoms corresponding to the W−O bonds; σ^2, the Debye−Waller factor; ΔE_0, the inner potential correction. Error bounds (accuracies) are estimated as N, ±5%; R, ±1%; σ^2, ±1%; ΔE_0, ±20%.

WO$_6$ octahedral units share their corners,[19] so as to form two different W−O bonds with lengths of 1.75 and 2.12 Å. In comparison with C-WO$_3$ and D-WO$_3$, the R-WO$_3$ with abundant oxygen vacancies possesses a reduced total coordination number (i.e., 5.4 versus 6.0). Specifically the reduction of coordination number mainly occurs at the longer W−O bonds, identifying the locations of oxygen vacancies. The absence of oxygen atoms at specific locations induces lattice disorder and dislocation.[18] In sharp contrast, the W atoms in D-WO$_3$ are coordinatively saturated despite the slightly altered proportion of two W−O bonds. The oxygen vacancies were further resolved by electron spin resonance (ESR) spectroscopy (Figure 1h), a tool for examining unpaired electrons in materials. The R-WO$_3$ uniquely exhibits a symmetrical ESR signal at $g = 2.002$, manifesting the electron trapping at oxygen vacancies.[20] Although a large number of oxygen vacancies were formed in R-WO$_3$, the valence state of W atoms has not been altered as indicated by X-ray photoelectron spectroscopy (XPS) (Figure S8). Taken together, the local structural information on R-WO$_3$ can be illustrated as Figure 1i.
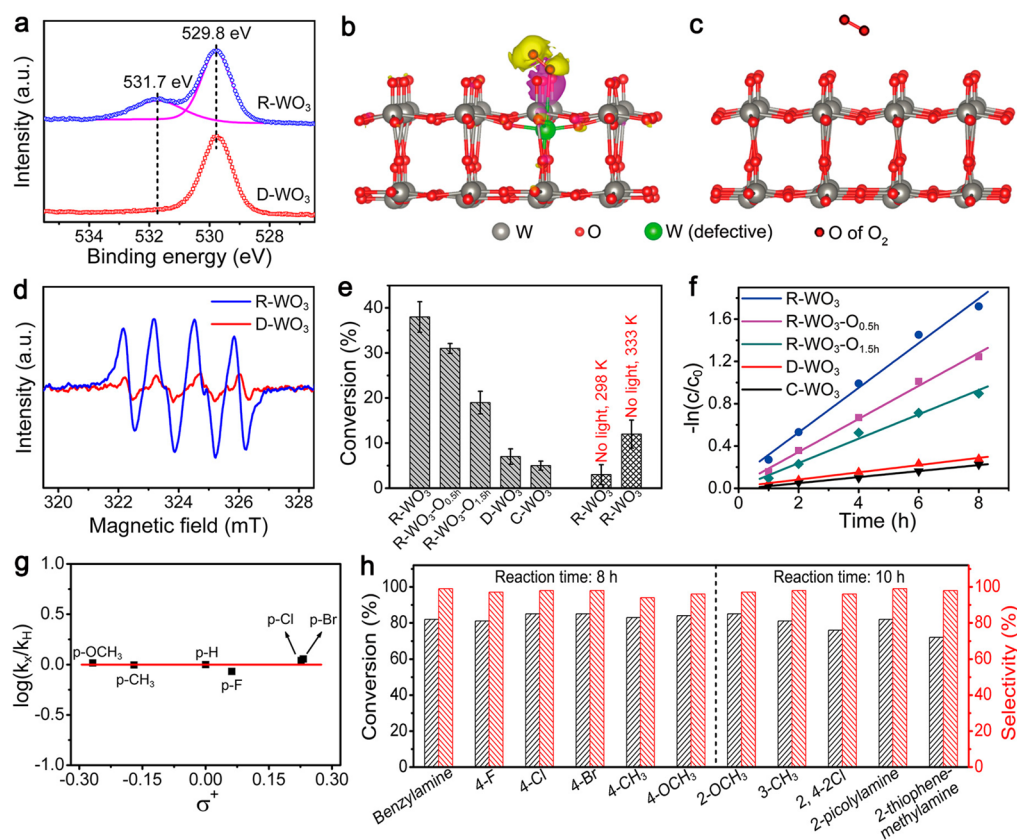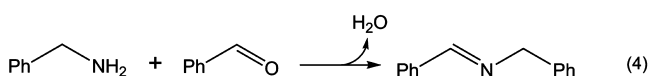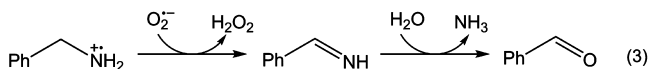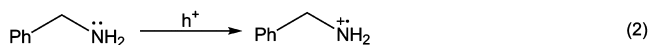
Figure 2. Oxygen activation and catalytic aerobic couplings by defective WO_3. (a) High-resolution O 1s XPS spectra of R-WO_3 and D-WO_3. Simulated differential charge density for (b) the O_2 chemisorbed at a CUS W site of defective WO_3, and (c) the O_2 adsorbed at the surface of perfect WO_3. The purple and olive colors represent increase and decrease in electron density, respectively, revealed by first-principles calculations. (d) ESR detection of superoxide radicals using a DMPO spin-trapping agent. The methanol solution of DMPO was preirradiated in the presence of R-WO_3 or D-WO_3. (e) Performance of various catalysts in aerobic coupling of benzylamine under irradiation of $\lambda > 400$ nm with thermostatic control at 298 K, in comparison with that by thermal process in the dark. Reaction time: 2 h. (f) Kinetic rate plots for light-driven catalytic aerobic coupling of benzylamine. (g) Hammett plots for light-driven catalytic aerobic couplings of substituted benzylamines using R-WO_3 as a catalyst. Reaction time: 1 h. (h) Conversion yield and selectivity for light-driven catalytic aerobic couplings of various benzylamine derivatives by R-WO_3. 4-F, 4-Cl, 4-Br, 4-CH_3, 4-OCH_3, 2-OCH_3, 3-CH_3, and 2,4-2Cl depict the substituent groups on benzene rings. Irradiation source and reaction temperature for (f–h): $\lambda > 400$ nm and 298 K.

The W atoms with low coordination numbers would provide CUS sites for oxygen species chemisorption. To resolve the chemisorption, we employed XPS to characterize the oxygen atoms involved in R-WO_3 and D-WO_3 (Figure 2a). The peak at 529.8 eV for both samples is attributed to the lattice oxygen ubiquitously in oxide semiconductors. Notably, an additional broad peak at 531.7 eV, arising from the oxygen species chemisorbed at oxygen vacancies, appears in the spectrum of R-WO_3. This also suggests that the oxygen vacancies are stabilized by the adsorbed oxygen species, a typical feature for the defect-rich oxides.[21] To gain insights into the species-catalyst interaction, we examined the adsorption of O_2 to WO_3 surface along with differential charge density using the density function theory.[22] Figure 2b illustrates that the O_2 is chemisorbed at the oxygen vacancy of defective WO_3 by taking an end-on configuration. The chemisorption is accompanied by a slight electron transfer from WO_3 CUS site to O_2 species. In comparison, a perfect WO_3 surface can hardly supply a site for the chemisorption of O_2 so as to defer their electronic coupling (Figure 2c). It is thus anticipated that the strong coupling between defective WO_3 and O_2, characterized by their electron transfer, would serve as a bridge to enable energy transfer from excitons to O_2 species once WO_3 is photoexcited.

Intuitively, the O_2 molecules accepting an additional electron can be activated into $O_2^{\bullet-}$; in our light-driven system, the provided electron is anticipated to originate from semiconductor photoexcitation. To trace the O_2 evolution, we employed 5,5-dimethyl-1-pyrroline N-oxide (DMPO), a typical spin-trapping agent for $O_2^{\bullet-}$, to examine the WO_3 samples in methanol.[23] In the dark, no $O_2^{\bullet-}$ was produced by WO_3 catalysts regardless of their oxygen vacancy concentrations (Figure S9). As we preirradiated the mixed solution of DMPO and WO_3, however, the ESR signals from $O_2^{\bullet-}$ captured by the DMPO, a nearly 1:1:1:1 quartet pattern, were observed (Figure 2d). Moreover, the signal intensities reveal that the R-WO_3 with oxygen vacancies can significantly better activate O_2 into $O_2^{\bullet-}$ species through electron transfer. This suggests that the chemisorption indeed can facilitate the energy transfer from excitons to O_2 species at the CUS sites of WO_3.

Based on the efficient exciton-O_2 energy transfer, the production of $O_2^{\bullet-}$ species provides a generic platform for O_2-participating catalytic reactions. As a demonstration, we employed aerobic organic couplings of amines to corresponding imines, the key components in various chemical manufacturing processes, as model reactions, in which interaction of C—H bonds with active oxygen species plays a critical role.[24,25] In the assessment, benzylamine was used as a

model substrate to react with $O_2^{\bullet-}$ species along the following pathway.[23,24]

$$O_2 \xrightarrow{e^-} O_2^{\bullet-} \qquad (1)$$

$$Ph\!-\!\overset{\displaystyle ..}{N}H_2 \xrightarrow{h^+} Ph\!-\!\overset{\displaystyle +\bullet}{N}H_2 \qquad (2)$$

$$Ph\!-\!\overset{+\bullet}{N}H_2 \xrightarrow[\;\;H_2O_2\;\;]{O_2^{\bullet-}} Ph\!-\!\overset{\displaystyle }{N}H \xrightarrow[\;\;NH_3\;\;]{H_2O} Ph\!-\!CHO \qquad (3)$$

$$Ph\!-\!NH_2 + Ph\!-\!CHO \xrightarrow[\;\;]{H_2O} Ph\!-\!N\!=\!Ph \qquad (4)$$

The reactions were proceeded in acetonitrile using O_2 as an oxidant under irradiation of $\lambda > 400$ nm at 100 mW·cm^{-2}, maintained at 298 K with thermostatic control. The yielded products were further analyzed by gas chromatography–mass spectrometry (GC-MS). To systematically correlate catalytic performance with oxygen vacancies, we prepared two additional reference samples, R-WO$_3$–O$_{0.5h}$ and R-WO$_3$–O$_{1.5h}$ (Figure S10), by recalcining R-WO$_3$ at 623 K in the air to gradually diminish oxygen vacancies. Figure 2e shows the light-driven catalytic performance in reactions by benchmarking R-WO$_3$ against a set of samples, with oxygen vacancy concentrations in order of R-WO$_3$ > R-WO$_3$–O$_{0.5h}$ > R-WO$_3$–O$_{1.5h}$ > D-WO$_3$ $\cong$ C-WO$_3$. It turned out that the conversion rates of benzylamine to N-benzylbenzaldimine had a strong correlation with the vacancy concentrations.

The performance was further quantified with the kinetic rate plots (Figure 2f), which regarded the aerobic coupling (Figure S11) as a pseudo-first order reaction.[26] Indeed, the reaction kinetics can be boosted by increasing the number of oxygen vacancies, manifesting their role as active sites. Remarkably, the calculated kinetic rate constant for R-WO$_3$ reached 0.211 h^{-1}, about 6 times higher than that of D-WO$_3$ (Table S2). Proceeded up to 2 h (Figure 2e), the reaction by R-WO$_3$ reached a conversion yield of 38%, well exceeding that by the

thermal process in the dark (e.g., 11% at 333 K). This suggests that the photoinduced electrons and holes may have altered the reaction pathway deviated from the thermal process. Nevertheless, the reaction efficiency still relies on the presence of oxygen vacancies in the thermally driven catalytic process (Table S3), demonstrating that surface vacancies provide indispensable active sites for the reactions.

Although we have well recognized the importance of catalyst oxygen vacancies to oxygen chemisorption and aerobic coupling, the relevance of the two processes still has to be proven. Table S4 shows that the O_2 concentrations hold the key to the efficiency of aerobic coupling. According to eq 3, the activated $O_2^{\bullet-}$ species should in turn react with benzylamine to produce an intermediate H_2O_2.[24,25] Such a H_2O_2 intermediate has been detected in our reaction system by a well-established N,N-diethyl-p-phenylenediamine (DPD)/horseradish peroxidase (POD) method (Figure S12). This further indicates that our reaction system has indeed followed the evolution process in eq 3. Looking into this reaction process, however, we have to point out that both O_2 activation and C–H bond cleavage should be accomplished to complete the reactions. To identify the rate-limiting step, we examined the α-C–H bond activation in benzylamine by graphing the Hammett plot with para-substituted benzylamines.[27] It turned out that the $\log(k/k_H)$ value was largely maintained as the Brown–Okamoto constants (σ^+) of side groups (MeO, Me, H, F, Cl, and Br) were altered (Figure 2g). This proves that the reaction does not undergo the process intermediated by carbocationic species so that the α-C–H bond cleavage is no longer the rate-limiting step in our light-driven catalytic process. As a result, such $O_2^{\bullet-}$ formation, achieved through our engineering on catalyst surface vacancy, can provide a generic approach to the aerobic couplings of various benzylamine derivatives with high selectivity (Figure 2h).

Upon gathering the above information, we can conclude that the O_2 activation is the key step to the entire reaction process.
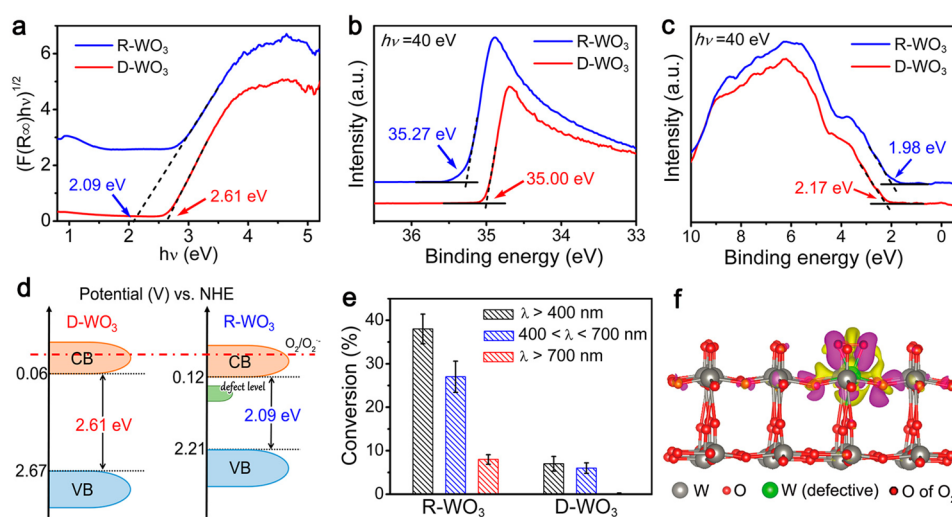

Figure 3. Defect-dependent electronic structure and photoexcited behavior. (a) Optical band gaps determined by UV–vis–IR diffuse reflectance spectra (Figure S13). (b) Secondary electron cutoff (E_{cutoff}) of the SRPES spectra. (c) Valence-band spectra measured by SRPES. (d) Schematics illustrating the electronic band structures. The reduction level for free $O_2^{\bullet-}$ radicals is marked by the red dash line. (e) Performance of R-WO$_3$ and D-WO$_3$ in catalytic aerobic coupling of benzylamine under various light irradiation at 298 K. Reaction time: 2 h. (f) Simulated differential charge density for the O_2 chemisorbed at a CUS W site of defective WO$_3$ upon charging an electron to the WO$_3$. Purple and olive colors represent increase and decrease in electron density, respectively.

In this sense, the high catalytic efficiency should mainly rely on the energy transfer from excitons inside WO_3 catalysts to O_2 species on surface. To depict the energy transfer process, we characterized the energy band structures of WO_3 nanosheets. As indicated by UV−vis−NIR diffuse reflectance spectra (Figure S13), creating oxygen vacancies not only extended light absorption toward longer wavelengths, but it also enabled remarkable NIR light harvesting. Based on the Tauc plot (Figure 3a), the band gaps of WO_3 nanostructures were narrowed from 2.61 to 2.09 eV, typically caused by defect engineering; the details for determining band gaps are included in the Supporting Information.[28,29] The energy band structures were further resolved by synchrotron radiation photoemission spectroscopy (SRPES, Figure 3b and c).[30] It is shown that the energy band structures of WO_3 are effectively tailored by defect engineering. As demonstrated in Figure 3b, the work functions (Φ) of R-WO_3 and D-WO_3, which are determined by the Fermi level (E_F), can be calculated to be 4.73 and 5.00 eV, respectively. Moreover, the valence band spectra show that the valence band maxima (VBMs) of R-WO_3 and D-WO_3 are 1.98 and 2.17 eV below the Fermi level (E_F), respectively (Figure 3c). Therefore, the D-WO_3 and R-WO_3 nanosheets turned out to have VBMs at 7.17 and 6.71 eV vs vacuum level, respectively. Base on the obtained band gaps and VBMs, the electronic band structures vs normal hydrogen electrode (NHE) can be determined as illustrated in Figure 3d.

To correlate the band structures with defects, we also performed first-principles simulations by creating an oxygen vacancy in WO_3 lattice (see simulation models in Figure S14). The computed partial densities of states (PDOS) diagrams (Figure S15) reveal that the conduction and valence band edges are primarily contributed by W 5d and O 2p orbitals, respectively. The unsaturated W atoms donate electrons to the O atoms around the oxygen vacancy,[31] elevating the potential of O 2p orbitals. This change in O 2p moves up valence band maximum (VBM) to narrow the band gap. Furthermore, the PDOS diagrams identify the emergence of defect states below conduction band minimum (CBM). The newly formed states would act as intermediate energy levels for lower-energy photoexcitation, enabling NIR light harvesting (>700 nm, Figure S13). The tunable light absorption in the NIR region significantly alters the sample color from light green to dark blue (Figure S16).

Interestingly, we notice that NIR light illumination ($\lambda > 700$ nm) makes a remarkable contribution to the entire light-driven catalytic performance by R-WO_3, whereas D-WO_3 exhibits nearly no activity (Figure 3e). Given the large exclusion of heat effect by thermostatic control, the NIR activity by R-WO_3 should be mainly ascribed to the carrier-participating reactions. This gives an exciting finding as the $O_2^{\bullet -}$ production should be thermodynamically disfavored in our case; both the CBM and defect states are positioned below the reduction level for free $O_2^{\bullet -}$ radicals ($O_2 + e^- \rightarrow O_2^{\bullet -}$, $E° = -0.33$ V vs NHE)[32] (Figure 3d). Then it is natural to ask how O_2 is efficiently activated at the CUS sites of WO_3 surface given this situation. As conduction and valence bands are contributed by different orbitals (Figure S17), the photogenerated electrons and holes would be mainly distributed at the CUS W atoms and the O atoms bonded to the neighbored W atoms, respectively. Our first-principles simulations (Figure 3f) reveal that the O_2 chemisorbed to a CUS W site switches to a side-on mode upon charging the WO_3 with an electron (which reflects the photoexcited state of WO_3). Consequently, the charged

defective WO_3 supplies 0.72 electrons to the chemisorbed O_2. Meanwhile, the O−O bond length is stretched from 1.22 to 1.47 Å, promoting the production of $O_2^{\bullet -}$. As the formation of free $O_2^{\bullet -}$ radicals is thermodynamically disfavored, it is assumed that the activated O_2 species is in a chemisorbed state at the surface vacancy (namely, $O_2^{* -}$). As such, the electrons can be effectively transferred from WO_3 catalysts to O_2 species, forming the $O_2^{* -}$. It is believed that such efficient electron transfer is enabled by the strong electronic coupling between O_2 species and CUS W atom. O K-edge near-edge X-ray absorption fine structure (NEXAFS) spectroscopy (Figure S18) has indicated the enhanced W−O bond covalency in defective WO_3, which may promote the coupling between W atoms and adsorbates through chemisorption, benefiting the electron transfer for the formation of $O_2^{* -}$.[33,34]

Another important finding is that our catalyst is free from the common concern that surface defects typically show low durability in catalytic reactions. Impressively, R-WO_3 nanosheets exhibited high performance stability in 6 catalytic cycles up to 48 h (Figure 4a), and well maintained their oxygen
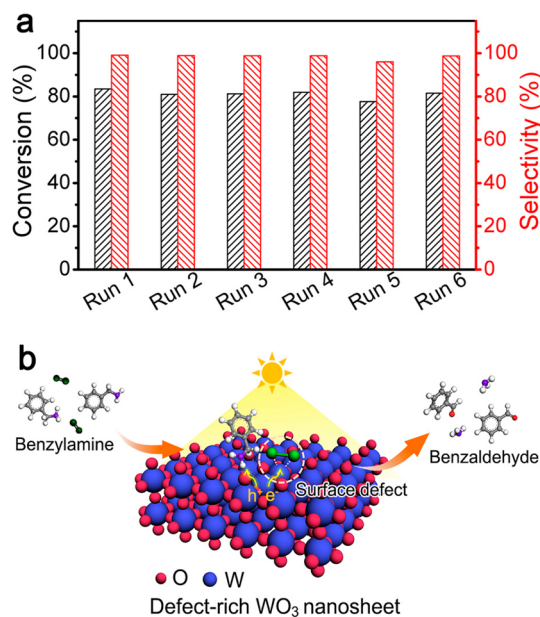

Figure 4. Catalytic durability and working mechanism for defect-rich WO_3. (a) Cyclic test for R-WO_3 in catalytic aerobic coupling of benzylamine under irradiation of $\lambda > 400$ nm at 298 K. Reaction time for each run: 8 h. (b) Schematic illustrating the entire light-driven catalytic reaction process.

vacancies during the reactions (Figure S19). To decode the mechanism responsible for excellent durability, we examined the other half reaction of aerobic coupling−activation of benzylamine by the photoexcited holes. As indicated by theoretical simulations (Figure S20), benzylamine molecules are adsorbed to the surface O atoms in neighbor to the defect; 0.76 holes will be transferred to the adsorbed benzylamine molecule when defective WO_3 is charged with a hole. The differential charge density further reveals that the C−H and N−H bonds are enriched with the transferred holes so as to activate the benzylamine by following the pathway in eq 3. The reaction of $O_2^{* -}$ at a CUS W site with the activated benzylamine nearby recovers the oxygen vacancy on catalyst surface, thereby enabling catalyst recyclability.

Upon elucidating the reaction process, we conclude the mechanistic pathway as illustrated in Figure 4b. The oxygen vacancies provide synergistic surface sites for accumulating the photogenerated electrons and activating the chemisorbed O_2, coupling the harvested solar energy into O_2 species. This holds the key to the overall aerobic coupling reaction. In the meantime, the photoexcited holes are distributed at the neighbored O atoms for benzylamine activation. The photogenerated electrons and holes are thereby well separated at different adsorption sites, overcoming the bottleneck in most light-driven catalytic organic reaction systems. The spatial locations of O_2^{*-} and benzylamine allow them to react to complete the entire process. In the mechanism, the electrons should be localized at the CUS W atoms for O_2 activation. This feature can be simply verified by delocalizing the electrons from CUS W sites using a Schottky junction. We photodeposited Au nanoparticles on R-WO$_3$ nanosheets to establish the Schottky junction while maintaining surface defects (Figure S21). Such a junction can efficiently trap the photoinduced electrons on Au.[35] Aligning well with our mechanism, the reduction of electron density at W sites substantially lowers catalytic efficiency indeed.

CONCLUSION

In conclusion, we have created the defects on WO$_3$ nanosheets, which provide numerous coordinatively unsaturated sites on surface for oxygen activation. The oxygen chemisorption enhanced at defect sites, which delivers charge carriers to the chemisorbed species, holds the key to the energy coupling of excitons with oxygen species. It enables the formation of superoxide radicals in a chemisorbed state (O_2^{*-}), which can in turn react with the amines adsorbed at the neighbor sites. As a result, the approach has efficiently coupled broadband sunlight into aerobic coupling of amines to corresponding imines, and enhanced the kinetic rate 6 times compared with defect-deficient WO$_3$. Furthermore, this photocatalyst can well tolerate the alteration of amine substrates and exhibit excellent stability in cyclic tests. This work thus clearly demonstrates that oxide defect engineering can serve as a versatile approach to refine catalysts, in efforts to develop solar-based chemical manufacturing at low material cost and energy consumption. The concept demonstrated here highlights the importance of chemisorption to utilization of excitons in solar-driven chemical transformation, and calls for future efforts on tailoring catalyst structures at atomic precision.

ASSOCIATED CONTENT

ⓈSupporting Information

The Supporting Information is available free of charge on the ACS Publications website at DOI: 10.1021/jacs.6b04629.

> Detailed experimental section, characterization methods, and additional material characterizations (PDF)

AUTHOR INFORMATION

Corresponding Authors
*yjxiong@ustc.edu.cn
*jiangj1@ustc.edu.cn

Author Contributions
†N.Z. and X.L. contributed equally.

Notes
The authors declare no competing financial interest.

REFERENCES

(1) Schultz, D. M.; Yoon, T. P. Science 2014, 343, 1239176.
(2) Yoon, T. P.; Ischay, M. A.; Du, J. Nat. Chem. 2010, 2, 527−532.
(3) Fukuzumi, S.; Kishi, T.; Kotani, H.; Lee, Y.-M.; Nam, W. Nat. Chem. 2011, 3, 38−41.
(4) Brongersma, M. L.; Halas, N. J.; Nordlander, P. Nat. Nanotechnol. 2015, 10, 25−34.
(5) Zahran, E. M.; Bedford, N. M.; Nguyen, M. A.; Chang, Y.-J.; Guiton, B. S.; Naik, R. R.; Bachas, L. G.; Knecht, M. R. J. Am. Chem. Soc. 2014, 136, 32−35.
(6) Christopher, P.; Xin, H.; Marimuthu, A.; Linic, S. Nat. Mater. 2012, 11, 1044−1050.
(7) Linic, S.; Aslam, U.; Boerigter, C.; Morabito, M. Nat. Mater. 2015, 14, 567−576.
(8) Bai, S.; Jiang, J.; Zhang, Q.; Xiong, Y. Chem. Soc. Rev. 2015, 44, 2893−2939.
(9) Kesavan, L.; Tiruvalam, R.; Ab Rahim, M. H.; bin Saiman, M. I.; Enache, D. I.; Jenkins, R. L.; Dimitratos, N.; Lopez-Sanchez, J. A.; Taylor, S. H.; Knight, D. W.; et al. Science 2011, 331, 195−199.
(10) Wittstock, A.; Zielasek, V.; Biener, J.; Friend, C.; Bäumer, M. Science 2010, 327, 319−322.
(11) Christopher, P.; Xin, H.; Linic, S. Nat. Chem. 2011, 3, 467−472.
(12) Romero, E.; Augulis, R.; Novoderezhkin, V. I.; Ferretti, M.; Thieme, J.; Zigmantas, D.; Van Grondelle, R. Nat. Phys. 2014, 10, 676−682.
(13) Scholes, G. D.; Fleming, G. R.; Olaya-Castro, A.; van Grondelle, R. Nat. Chem. 2011, 3, 763−774.
(14) Zuo, F.; Wang, L.; Wu, T.; Zhang, Z.; Borchardt, D.; Feng, P. J. Am. Chem. Soc. 2010, 132, 11856−11857.
(15) Gordon, T. R.; Cargnello, M.; Paik, T.; Mangolini, F.; Weber, R. T.; Fornasiero, P.; Murray, C. B. J. Am. Chem. Soc. 2012, 134, 6751−6761.
(16) Cheng, H.; Kamegawa, T.; Mori, K.; Yamashita, H. Angew. Chem., Int. Ed. 2014, 53, 2910−2914.
(17) Tada, H.; Mitsui, T.; Kiyonaga, T.; Akita, T.; Tanaka, K. Nat. Mater. 2006, 5, 782−786.
(18) Sun, Y.; Liu, Q.; Gao, S.; Cheng, H.; Lei, F.; Sun, Z.; Jiang, Y.; Su, H.; Wei, S.; Xie, Y. Nat. Commun. 2013, 4, 2899.
(19) Zheng, H.; Ou, J. Z.; Strano, M. S.; Kaner, R. B.; Mitchell, A.; Kalantar-zadeh, K. Adv. Funct. Mater. 2011, 21, 2175−2196.
(20) Lei, F.; Sun, Y.; Liu, K.; Gao, S.; Liang, L.; Pan, B.; Xie, Y. J. Am. Chem. Soc. 2014, 136, 6826−6829.
(21) Banger, K.; Yamashita, Y.; Mori, K.; Peterson, R.; Leedham, T.; Rickard, J.; Sirringhaus, H. Nat. Mater. 2011, 10, 45−50.
(22) Kresse, G.; Furthmüller, J. Phys. Rev. B: Condens. Matter Mater. Phys. 1996, 54, 11169−11186.
(23) Su, C.; Acik, M.; Takai, K.; Lu, J.; Hao, S.-j.; Zheng, Y.; Wu, P.; Bao, Q.; Enoki, T.; Chabal, Y. J.; Ping Loh, K. Nat. Commun. 2012, 3, 1298.
(24) Su, F.; Mathew, S. C.; Möhlmann, L.; Antonietti, M.; Wang, X.; Blechert, S. Angew. Chem., Int. Ed. 2011, 50, 657−660.

(25) Lang, X.; Chen, X.; Zhao, J. *Chem. Soc. Rev.* **2014**, *43*, 473−486.

(26) Lang, X.; Ji, H.; Chen, C.; Ma, W.; Zhao, J. *Angew. Chem., Int. Ed.* **2011**, *50*, 3934−3937.

(27) Brown, H. C.; Okamoto, Y. *J. Am. Chem. Soc.* **1958**, *80*, 4979−4987.

(28) Chen, X.; Liu, L.; Yu, P. Y.; Mao, S. S. *Science* **2011**, *331*, 746−750.

(29) Li, L.; Yan, J.; Wang, T.; Zhao, Z.-J.; Zhang, J.; Gong, J.; Guan, N. *Nat. Commun.* **2015**, *6*, 5881.

(30) Liu, J.; Liu, Y.; Liu, N.; Han, Y.; Zhang, X.; Huang, H.; Lifshitz, Y.; Lee, S.-T.; Zhong, J.; Kang, Z. *Science* **2015**, *347*, 970−974.

(31) Naldoni, A.; Allieta, M.; Santangelo, S.; Marelli, M.; Fabbri, F.; Cappelli, S.; Bianchi, C. L.; Psaro, R.; Dal Santo, V. *J. Am. Chem. Soc.* **2012**, *134*, 7600−7603.

(32) Wood, P. M. *Biochem. J.* **1988**, *253*, 287−289.

(33) Suntivich, J.; Gasteiger, H. A.; Yabuuchi, N.; Nakanishi, H.; Goodenough, J. B.; Shao-Horn, Y. *Nat. Chem.* **2011**, *3*, 546−550.

(34) Suntivich, J.; May, K. J.; Gasteiger, H. A.; Goodenough, J. B.; Shao-Horn, Y. *Science* **2011**, *334*, 1383−1385.

(35) Linsebigler, A. L.; Lu, G.; Yates, J. T., Jr *Chem. Rev.* **1995**, *95*, 735−758.